Mo-doped SnO$_2$ Mesoporous Hollow Structured Spheres as Anode Materials for High-Performance Lithium Ion Batteries

Xuekun Wang, Zhaoqiang Li, Zhiwei Zhang, Qun Li, Enyan Guo, Chengxiang Wang*, Longwei Yin*

Key Laboratory for Liquid-Solid Structural Evolution and Processing of Materials, Ministry of Education, School of Materials Science and Engineering, Shandong University, Jinan 250061, P. R. China

*To whom correspondence should be addressed. Tel.: + 86 531 88396970. Fax: + 86 531 88396970. E-mail: yinlw@sdu.edu.cn

ABSTRACT: We designed a facile infiltration route to synthesize mesoporous hollow structured Mo doped SnO$_2$ using silica spheres as templates. It is shown that Mo is uniformly incorporated into SnO$_2$ lattice in form of Mo^{6+}. The as-prepared mesoporous Mo-doped SnO$_2$ LIBs anodes exhibit a significantly improved electrochemical performance with good cycling stability, high specific capacity and rate capability. The mesoporous hollow Mo-doped SnO$_2$ sample with 14 at% Mo doping content displays a specific capacity of 801 mAhg^{-1} after 60 cycles at a current density of 100 mAg^{-1}, about 1.66 times higher than that of pure SnO$_2$ hollow sample. In addition, even as the current density is high as 1600 mAg^{-1} after 60 cycles, it could still retain a stable specific capacity of 530 mAhg^{-1}, exhibiting an extraordinary rate capability. The greatly improved electrochemical performance of Mo-doped mesoporous hollow SnO$_2$ sample could be attributed to the following issues. The large surface area and hollow structure can significantly enhance the structural integrity by acting as mechanical buffer, effectively alleviate the volume changes generated during lithiation/delithiation process. The incorporation of Mo into lattice of SnO$_2$ can improve charge transfer kinetics and results in a faster Li$^+$ diffusion rate during the charge-discharge process.

Keywords: SnO$_2$; doping; lithium ion battery; anode; porous

1. Introduction

Lithium ion batteries (LIBs) have attracted much attention as important power sources for many portable electronic devices due to their superior specific energy, excellent rate capability, environmental friendliness and low cost.[1-3] However, the currently commercial graphite anode materials display only a limited theoretical specific capacity of 372 mAhg^{-1} and poor rate capability. To meet the continuous demands for electrochemical energy storage with higher energy density and better cycling performance to power advanced portable electronic devices and newly emerging communication facilities, transition metal oxides have been intensively explored as future anode materials for LIBs due to their high energy density. Among these materials, tin dioxide (SnO_2) is a promising candidate for anode materials of LIBs, owing to its high theoretical capacity (790 mAhg^{-1}), good processibility, widespread availability and low toxity.[4, 5]

Regardless of high theoretical specific capacity, the potentially commercial application of SnO_2 as a LIBs anode is still greatly blocked by some practical problems, such as poor cycling stability and poor electronic conductivity.[6] In the field of metal oxide anode materials, the former problem is highly common, and is well known to be caused by the huge volume change of more than 200% upon lithium insertion/extraction process. Special endeavors have been devoted to accommodate volume changes and the pulverization effect that occurs during lithiation and delithiation process. One effective strategy is to design nano-architecture tin oxide materials, such as nanotubes[7,8], nanofilms[9-11] and hollow spheres.[12-14] Among the nanostructured morphologies, hollow nanostructures show their superiority to mitigate volume changes and pulverization effect. Prompted by the benefit, nano-sized hollow and/or porous materials have been consumingly investigated as LIBs anode materials.

The electrochemical properties of electrode materials could be further improved by enhancing electrical conductivity. One of the most commonly used techniques is to design SnO_2-based composites with conducting materials such as with carbonaceous materials and conducting polymers to improve the electrical conductivity and alleviate the volumetric strain generated during lithiation/delithiation cycling.[13,15,16] Another general approach is to alter the intrinsic conductivity of SnO_2 via metal cationic doping. Cationic doping has been considered to be an effective strategy to improve electrical conductivity of metal oxide anode materials. Prompted by above benefit, extensive works have been carried out on various metal cationic doping (such as Sb,[17, 18] Co,[19] Cu,[20-22] Mo[23, 24] and Ti[25]) to improve lithium storage properties of metal oxide LIBs anode materials. Previous studies have shown that cation doped SnO_2 anode materials exhibit enhanced electrochemical performance. Wang's group[17] reported that the discharge capacity of Sb-doped SnO_2 microspheres can still maintain at 227 mAhg^{-1} after 50 cycles. In 2013, Rogach et al.[25] reported that Ti-doped SnO_2 nanowires still deliver a high discharge capacity of 319 mAhg^{-1} at a current density of 250 mAg^{-1} after 35 cycles. To our best knowledge, the Mo-doped hollow structured SnO_2

anode material was rarely reported.

Herein, we design a facile infiltration route to prepare hollow structured Mo-doped SnO_2 (MTO) materials with controlled morphology using silica spheres as templates, $SnCl_2 \cdot 2H_2O$ as Sn precursor and ammonium heptamolybdate (AHM) as Mo source. Mo dopant is uniformly distributed among the MTO materials, and incorporated into SnO_2 lattice in the form of Mo^{6+}. The as-prepared Mo-doped SnO_2 anode samples exhibit a significantly improved cycling stability and rate capability. Electrochemical analysis results reveal that SnO_2 hollow spherical sample doped with 14 at% Mo (MTO-1) displays a high specific capacity up to 801 mAhg^{-1} after 60 cycles at a high current density of 100 mAg^{-1} (about 1.66 times larger than that of non-doped sample). In addition, even at the current density as high as 1600 mAg^{-1} after 60 cycles, it could still retain a stable specific capacity of 530 mAhg^{-1}, exhibiting an extraordinary rate capability performance. It is shown that Mo doping into SnO_2 greatly improves electrochemical performance of LIBs anode materials and could find potential applications.

2. Experimental section

2.1 Synthesis of silica spheres

Silica spheres was prepared by the modified Stober method.[26] In a typical synthesis, 110 mL of ethanol and 18 ml of 28% ammonium hydroxide were first mixed under vigorous stirring. After 5 min, 7.5 g TEOS was added to the above homogeneous solution. Then, the mixture was magnetically stirred for 10 h at room temperature. The as-prepared products were centrifuged, washed with deionized water, and dried at 323 K.

2.2 Synthesis of molybdenum doped tin dioxide (MTO)

Mo doped SnO_2 materials were prepared as following process. Firstly, 1.53 g of $SnCl_2 \cdot 2H_2O$ was melted to liquid phase at 353 K. Then 1.0 g of silica spheres was added under vigorously stirring. Afterward, 5 g of deionized water and predetermined quantities of ammonium heptamolybdate (AHM) were dissolved into above mixture and sonicated for about 10 min to form a homogeneous sol. The Mo:Sn molar ratio used is 0:1, 1:8, and 1:5, respectively. Then, the composite materials were put into an oven at 353 K for 36 h in order for the infiltration of tin precursor within the pores of silica spheres. Afterwards, the materials were heated at 973 K for 3 h in tube furnace. Subsequently, the prepared products were added into an aqueous solution of HF (20 wt%) under stirring, centrifuged, washed with deionized water to remove the silica, then dried at 353 K in vacuum for 8 h. Finally, after drying process, Mo doped SnO_2 products were obtained. The samples prepared with different Mo:Sn molar ratios (0:1, 1:8, and 1:5) were denoted as MTO-0, MTO-1 and MTO-2 samples, respectively.

2.3 Material characterization

The structure and morphology of materials were characterized by X-ray diffraction (XRD; Rigaku D/Max-KA, Cu *Ka*), field emission scanning electron microscopy (FESEM: SU-70), and high resolution transmission electron microscopy (HRTEM: JEM-2100, 200 kV). Nitrogen adsorption-desorption isotherms were determined at 77 K using Gold APP V-Sorb 2800 surface area and porosity analyzer. The surface area measurements were performed according to the Brunauer-Emmett-Teller (BET) method. The pore size distribution was obtained from the desorption branch of isotherm using the corrected form of Kelvin equation by means of the Barrett-Joyner-Halenda (BJH) method. X-ray photoelectron spectroscopy (XPS, ESCALAB 250 with 200 W Al Ka probe beam) was used to characterize the surface chemical composition information of the products. Binding energies (BE) were calibrated with the C 1s reference peak at 284.7 ev.

2.4 Electrochemical Measurements

The electrochemical measurements were conducted via standard CR2025 coin-type cells fabricated in a glove box under an argon atmosphere. Copper foil was used as the current collectors, while lithium foil as reference electrodes and 1.0 M $LiPF_6$ in mixed ethylene carbonate (EC) and diethyl carbonate (DEC) (EC:DEC, 1:1 by volume) as the electrolyte. A cut-off voltage window of 0.01-3.0 V is used. The working electrode consisted of 70wt% active material (MTO-0, MTO-1 and MTO-2), 15wt% carbon black (super-P-Li) and 15wt% polyvinylidene difluoride (PVDF). The mass of active materials in electrodes is 1 mg. Cells were discharged and charged on a LAND CT2001A system (Wuhan, China) at room temperature. Cyclic voltammetry (CV) tests were conducted on an electrochemical workstation (PARSTAT 2273) between 0.01-3.0 V at a scan rate of 0.1 mV s^{-1}.

3. Results and Discussion

The crystal structure of the as-prepared MTO samples is examined by x-ray diffraction (XRD). Fig. 1a shows wide-angle XRD patterns of MTO samples with different Mo doping contents. The diffraction peaks of the MTO-0 sample can be well indexed to tetragonal rutile SnO_2 (JCPDS 41-1445) without any other impurities. With Mo doping addition, the lattice structure of SnO_2 is not destroyed. Both the XRD patterns of MTO-1 and MTO-2 samples are basically assigned to the tetragonal rutile SnO_2 (JCPDS: 41-1445), and no obvious peaks of molybdenum oxides and other impurities were detected. However, with the addition of Mo into lattice of MTO, the diffraction peaks of MTO samples shift to the position at larger angles. Fig. 1b shows the magnified (110) diffraction peak of MTO samples, clearly revealing that (110) peak shifts right to position at higher angles. To further investigate the effect of doping on the lattice structure of SnO_2, lattice parameters of the MTO samples were calculated using the Brag equation from the diffraction peaks of (110). The unit cell parameters of MTO samples are listed in Table 1. The lattice constants is a = 4.7467 Å and c = 3.1839 Å for pure SnO_2 sample (MTO-0). For Mo-doped SnO_2 samples MTO-1 and MTO-2, the lattice parameters are determined as 4.743×3.180

Å and 4.736×3.184 Å, respectively. For the three MTO samples, the cell volume decreases with the increase of the Mo content, which is due to smaller radius of Mo^{6+} ion (0.059 nm) than that of Sn^{4+} ion (0.069 nm). Meanwhile，its higher valence state may lead to the formation of cation vacancies in order to maintain the electron neutrality of the crystal cell.

The elemental composition of the MTO-1 sample was further characterized by X-ray photoelectron spectroscopy (XPS) using the C 1s peak at 284.7 eV as the reference peak. The XPS spectra of the MTO-1 sample are shown in Fig. 2. The survey spectrum (Fig. 2a) reveals that the sample contains only O, Sn and Mo elements. Fig. 2b-d depicts high-resolution XPS spectra of individual elements. Fig. 2b shows XPS spectrum of O 1s, suggesting three peaks located at 531.75, 530.63 and 530.05 eV, respectively. The peak centered at 531.75 ev is originated from the oxygen deficient center in the matrix of SnO_2.[27,28] The other two bands are ascribed to the O^{2-} ion in the SnO_2 tetragonal rutile, surrounded by Sn (or the substitution of Mo) atoms with their full complement of nearest-neighbor O^{2-} ions.[29-32] Fig. 2c displays high-resolution XPS spectrum of Sn 3d, the two symmetric peaks located at 494.9 and 486.5 eV can be attributed to Sn $3d_{3/2}$ and Sn $3d_{5/2}$ lines, respectively. The lower binding energy of Sn $3d_{5/2}$ of MTO-1 sample than that of pure SnO_2, could be attributed to oxygen deficiency resulted by the Mo doping.[33, 34] As shown in Fig. 2d, the Mo $3d_{3/2}$ and Mo $3d_{5/2}$ peaks located at 235.6 and 232.4 ev are similar to that obserbed in MoO_3, implying that the formal oxidation state of Mo in SnO_2 is +6.[35]

The nitrogen adsorption-desorption isotherms and the corresponding pore size distribution curves by the BJH method of the MTO samples are shown in Fig. 3. As shown in Fig. 3a, all the samples exhibit type Ⅳ characteristic with an obvious capillary condensation step, indicating the presence of a pronounced inter-particle mesopore size distribution. The textural properties of the MTO materials are listed in Table 2. The synthesized pure SnO_2 (MTO-0) exhibits a specific surface area of 26.20 m^2g^{-1} and a pore volume of 0.3 cm^3g^{-1}, respectively, with an average pore size of 38.39 nm. With the addition of Mo, the MTO-1 sample displays a surface area of 103.31 m^2g^{-1} and pore volume 0.46 cm^3g^{-1}, respectively. Nevertheless, with the Mo content increasing, the specific surface area and pore volume of MTO-2 sample decrease to 48.72 m^2g^{-1} and 0.26 cm^3g^{-1}, respectively.

The microstructure and surface morphology of the as-prepared samples are studied in a field emission scanning electron microscope (FESEM), as shown in Fig. 4. SiO_2 spheres with uniform morphology are revealed in Fig. 4a-4b. Fig. 4c-h depict SEM images of MTO samples with different Mo-doping contents, clearly suggesting the presense of the hollow stucture for the synthesized materials. The diameter of MTO-1 and MTO-2 hollow products is about 300 nm, which is coincident with the size of SiO_2 spherical templates. The elemental composition of the MTO-1 samples was further examined via x-ray energy-dispersive spectroscopy (EDS) and EDS mapping characterization, as shown in Fig. 5 and Fig. 6. The EDS spectrum in Fig. 5 reveals that the MTO-1

sample is composed of Mo, Sn and O elements. Elemental mapping images in Fig. 6 clearly demonstrate that Mo, Sn, O elements are uniformly distributed throughout the whole MTO-1 sample.

Transmission electron microscopy (TEM) is applied to further investigate the detailed microstructures of the synthesized MTO-1 sample (Fig. 7). From low magnification TEM images shown in Fig. 7a-7b, it is clearly shown that the diameter of the spherical MTO-1 samples is about 300 nm, which is in well agreement with FESEM results. The crystal structure of the MTO-1 sample can be determined by electron diffraction (ED) pattern in Fig. 7c, suggesting the polycrystalline nature for the synthesized MTO-1 sample. The diffraction rings in the typical ED pattern correspond well with (110), (101), (211), (301) planes of tetragonal rutile structured SnO_2 (space group: *P42/mnm*) with lattice constants of a = 4.74 Å and c = 3.19 Å. Fig. 7d-7e gives typical HRTEM lattice images of the MTO-1 samples, suggesting the MTO-1 sample is composed of highly crystalline nanoparticles with a diameter of 5 nm. It should be noted that there exists mesopores in the MTO-1 sample in a range of 2-5 nm, which is useful to alleviate the volume changes during cycles (Fig. 7d). Fig. 7f depicts a typical lattice HRTEM image taken along [212] zone axis. The marked d-spacing of 2.12 Å and 2.65 Å in the lattice image corresponds well with that of (1-20) and (-101) planes of tetragonal rutile SnO_2, in consistent with the data acquired by the XRD result.

The electrochemical performance of the synthesized MTO materials is investigated as anode materials for LIBs. Fig. 8 shows the initial five charge-discharge curves between 0.01 V and 3 V at a current density of 100 mAg^{-1} for the MTO anode electrodes. With the addition of Mo dopant content increasing, the Mo-doped SnO_2 products display remarkably increased initial reversible capacity. The initial discharge capacity of MTO-0, MTO-1 and MTO-2 samples is 1978, 2088 and 2155 mAhg^{-1}, and initial charge capacity is 1059, 1256 and 1368 mAhg^{-1}, respectively, corresponding to initial coulombic efficiency of 53.5, 60 and 63.5%, respectively. At 5th cycle, the discharge capacity of MTO-0, MTO-1 and MTO-2 products is 856, 1114 and 1060 mAhg^{-1}, respectively. It is shown that it is an effective strategy to improve the specific capacity and initial coulombic efficiency of SnO_2 via Mo^{6+} cationic doping.

Figure 9 displays the cyclic voltammogram (CV) curves of the first five cycles of the MTO electrodes at a slow scan rate of 0.1 mVs^{-1} between 0.01-3.0 V. In the first cycle, two broad reduction peaks can be observed at 0.85 V and 0.19 V for the MTO-0 sample (Fig. 9a). The 0.85 V peak could be attributed to the formation of a solid electrolyte interphase (SEI) layer on the active sample surface (reaction 1), and the transformation of SnO_2 and Li^+ to metallic Ti and amorphous lithium oxide (reaction 2). The 0.19 eV peak could be ascribed to the formation of different Li_xSn alloy phases (reaction 3).

$Li^+ + e^- + electrolyte \rightarrow SEI (Li)$ (1)

$$SnO_2 + 4Li^+ + 4e^- \rightarrow Sn + 2Li_2O \qquad (2)$$

$$Sn + xLi^+ + xe^- \rightarrow Li_xSn \ (0 < x < 4.4) \quad (3)$$
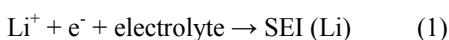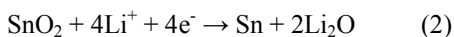
In the first anodic sweep, two anodic peaks, namely, one main peak at about 0.56 V and one weak but broad peak between 1.1 and 1.3 V, are observed. The peak at about 0.56 V corresponds to the dealloying process of Li_xSn alloy during the cathodic scan. It is generally accepted that the first two reactions are believed to be irreversible. However, it is worth mentioning that an broad anodic peak centered at 1.23 V could be most likely owing to the oxidation of Sn to SnO_2. therefore, reaction 2 is reversible to some extent.[36-39] These results are in good agreement with previous reports.[39-41]

For the Mo doped SnO_2, the shape of the CV curves is similar to that of pure SnO_2 sample. All the redox peaks are observable in both the CV curves of MTO-1 (Fig. 9b) and MTO-2 (Fig. 9c) samples. For MTO-1 electrode, the initial reduction peaks shift to 0.037 and 0.77 V, respectively, and the oxidation peaks shift to 0.59 and 1.25 V, respectively. It is found that the intensity of anodic peaks for MTO-1 electrode are much stronger than that of pure SnO_2 (MTO-0) electrode, which can be mainly ascribed to the improved electronic conductivity of MTO-1 electrode. In addition, the integral areas of the MTO-1 electrode are larger than that of MTO-0 electrode, implying the improvement of electrochemical activity with Mo doping in SnO_2. In the subsequent cycles, the CV curves almost overlap each other, suggesting a good cyclability of the MTO-1 electrode.

The electrochemical impedance spectroscopy (EIS) was used to comparatively investigate the charge transport kinetics of MTO electrode samples. Fig. 10 depicts the Nyquist plots of the AC impedance for the MTO samples, which are obtained at an open circuit voltage state using fresh cells. As shown in Fig. 10, all the curves are consisted of a semicircle in the high to medium frequency and a sloping line in the low frequency. The diameter of the semicircle in the high to medium frequency region on Z_{re} axis is related to the ohmic resistance and charge transfer resistance, providing an approximate indication of the charge transfer resistance on electrode-electrolyte interface (Rct).[42] The diameter of the semicircle of Mo-doped SnO_2 materials, especially MTO-1 sample, is much smaller than that of pure SnO_2 electrode, indicating that the charge transfer resistance decreases drastically, reflecting the incorporation of Mo into SnO_2 materials can facilitate electron transfer and Li^+ ion charge transfer at the interface between the electrode and electrolyte. The inclined line in the low frequency is connected with the diffusion coefficient of lithium ions in the anode materials. By comparing the slopes of all the straight lines in low frequency, it is suggested that Mo-doped SnO_2 samples display a larger Li^+ ion diffusion coefficient than that of undoped sample.

Galvanostatic technique is utilized to study the charge-discharge cycling performance of the MTO electrodes at a current density of 100 mAg^{-1}. Fig. 11 comparatively depicts the profiles of capacity vs. cycle number curves of

7

the MTO-0, MTO-1 and MTO-2 electrodes. It is obviously indicated that the MTO-1 electrode exhibits much better cycling performance than the MTO-0 and MTO-2 electrodes. The MTO-1 and MTO-2 electrodes display an initial discharge capacity of 2088 and 2155 mAhg^{-1}, and reversible capacity of 1256 and 1368 mAhg^{-1}, respectively, exhibiting improved specific capacity in comparison with that of pure SnO_2 sample. The initial discharge and charge capacity of pure SnO_2 sample (MTO-0) are 1978 and 1059 mAhg^{-1}, respectively, with an initial coulombic efficiency of 53.5%. Compared with MTO-1 sample, during the first 15 cylcels, the reversible capacity of MTO-2 and MTO-0 samples drops quickly, decreasing to 750 and 655 mAhg^{-1}, respectively at the 15th cycle. While MTO-1 sample can maintain a reversible capacity of 901 mAhg^{-1} at the 15th cycle. During 15-20 cycles, the reversible capacity of MTO-1 sample drops gradually, while reversible capacity of MTO-2 and MTO-0 samples still drops faster with cycle time increasing. After that, the reversible capacity of MTO-1 sample almost does not change with cycle time increasing, while reversible capacity of MTO-2 and MTO-0 samples decreases all the way. At the 60th cylce, MTO-1 displays a reversible capacity of 801 mAhg^{-1}, much higher than that the reversible capacity of 525 and 477 mAhg^{-1} for MTO-2 and MTO-0 samples. It is distinctly indicated that MTO-1 sample shows a much more excellent cyclability than that of previously reported SnO_2-based materials. For example, Hyeon's group reported a capacity of 380 mAhg^{-1} for the hollow SnO_2 microspheres at a current density of 100 mAg^{-1} after 40 cycles.[51] While SnO_2-carbon hollow spheres display a reversible capacity of 473 mAhg^{-1} after 50 cycles.[21] Wang's team[17] reported that a capacity of Sb doped SnO_2 microspheres can be remained at 227 mAhg^{-1} after 50 cycles. While the reported Ti-doped SnO_2 nanowire anode exhibits a capacity of 319 mAhg^{-1} after 35 cycles at a current density of 250 mAg^{-1}.[25]

Moreover, the MTO-1 electrode exhibits superior performance of rate capability (Fig. 13). At a rate of current density of 50 mAg^{-1}, the discharge capacity remains at 1023 mAhg^{-1} after 10 cycles. At the 20 cycles at a current density of 100 mAg^{-1}, the discharge capacity can retain at 831 mAhg^{-1}. As the cycle reaches 40th cycles, the MTO-1 sample remains a reversible capacity of 649 mAhg^{-1} at a current density of 400 mAg^{-1}. Even at a high charge rate of 1600 mAg^{-1} after 60 cycles, MTO-1 sample still keeps a stable reversible capacity of 530 mAhg^{-1}, which is approximately about 2.86 times higher than that of MTO-0 (185 mAhg^{-1}). In addition, it should be noted that as the current density returns back to 50 mAg^{-1}, the specific capacity of MTO-1 electrode can nearly return to the original capacity, still maintaining at 893 mAhg^{-1} after 70 cycles, much better than that of pure SnO_2 (675 mAhg^{-1}). It is confirmed that MTO-1 electrode could keep its integrity for a long number of cycles as well as at high rates.

As shown above, the Mo-doped SnO_2 samples exhibit significantly improved cycling performance and remarkably high rate capability. The greatly improved electrochemical performance of high reversible specific

capacity, enhanced cycling stability and high-rate capability of MTO-1 sample could be attributed to the unique microstructure characteristics and cationic doping effect of the Mo-doped SnO_2 samples. (i) It is shown that the MTO-1 displays a high surface area of 103.31 m^2g^{-1}, and the spherical MTO-1 sample shows a hollow structure with a small shell thickness and a large interior hollow space. TEM images also indicate that there exists large amounts of mesopores about 2-5 nm among the SnO_2 nanoparticles. The large surface area, macropores and mesopores can significantly enhance the structural integrity by acting as mechanical buffer, effectively alleviate the volume changes generated during lithiation and delithiation process. (ii) According to above EIS analysis, due to the incorporation effect of Mo into lattice of SnO_2, the charge-transfer impedance of the MTO-1 electrodes greatly decreases, resulting in improved charge transfer kinetics and faster Li ion diffusion rate with improved reaction rate during the charge-discharge process. (iii) TEM images reveal that the MTO-1 sample is composed of highly crystalline smaller nanoparticles with a uniform size of 3-4 nm, the smaller nanosized effect and highly crystalline of M-doped SnO_2 can be useful to enhance the elelctrochemical performance of the MTO-1 sample as anode materials fro LIBs. (Vi) It is generally considered that Li-ion diffusion is mainly dependent on the transport length and accessible sites on the surface of active materials. So, the large surface area, the presence of mesopores, macropores can effectively increase the electrode/electrolyte contact area, short path length for Li transport. Therefore, it is expected that the MTO-1 sample offers improved energy storage capacity, Coulombic efficiency, better cycling stability and high rate capability.

4. Conclusions

In summary, we developed a facile infiltration route to prepare hollow structured Mo-doped SnO_2 (MTO) materials with controlled morphology using silica spheres as templates, $SnCl_2 \cdot 2H_2O$ as tin precursor and ammonium heptamolybdate (AHM) as molybdenum source. Mo dopant is uniformly distributed among the MTO materials, and incorporated into SnO_2 lattice in the form of Mo^{6+}. Electrochemical results revealed that SnO_2 hollow spheres doped with 14 at% Mo (MTO-1) exhibit a significantly improved cycling stability and rate capability. At a current density of 100 mAg^{-1}, MTO-1 displays a high specific capacity up to 798 $mAhg^{-1}$ after 60 cycles at a high current density of 100 mAg^{-1} (about 1.66 times larger than that of non-doped sample). In addition, even at the current density as high as 1600 mAg^{-1} after 60 cycles, it could still retain a stable specific capacity of 530 $mAhg^{-1}$, exhibiting an extraordinary rate capability performance. It is shown that Mo doping into SnO_2 greatly improves electrochemical performance of LIBs anode materials and could find potential applications. The greatly improved electrochemical performance of MTO-1 sample could be ascribed to advantageous hollow

interior space, highly crystalline and smaller size of Mo-doped SnO_2 nanoparticles, and cationic doping of Mo into lattice of SnO_2 to enhance the charge transfer kinetics.

Acknowledgments

References

1. L. Ji, Z. Lin, M. Alcoutlabi and X. Zhang, *Energ Environ Sci*, 2011, **4**, 2682-2699.

2. B. J. Landi, M. J. Ganter, C. D. Cress, R. A. DiLeo and R. P. Raffaelle, *Energ Environ Sci*, 2009, **2**, 638-654.

3. M. G. Kim and J. Cho, *Adv Funct Mater*, 2009, **19**, 1497-1514.

4. I. A. Courtney and J. R. Dahn, *J Electrochem Soc*, 1997, **144**, 2045-2052.

5. C.-M. Wang, W. Xu, J. Liu, J.-G. Zhang, L. V. Saraf, B. W. Arey, D. Choi, Z.-G. Yang, J. Xiao, S. Thevuthasan and D. R. Baer, *Nano Lett*, 2011, **11**, 1874-1880.

6. J. M. Tarascon and M. Armand, *Nature*, 2001, **414**, 359-367.

7. J. Ye, H. Zhang, R. Yang, X. Li and L. Qi, *Small*, 2010, **6**, 296-306.

8. P. Wu, N. Du, H. Zhang, J. Yu, Y. Qi and D. Yang, *Nanoscale*, 2011, **3**, 746-750.

9. C. Wang, Y. Zhou, M. Ge, X. Xu, Z. Zhang and J. Z. Jiang, *J Am Chem Soc*, 2009, **132**, 46-47.

10. X. J. Zhu, Z. P. Guo, P. Zhang, G. D. Du, R. Zeng, Z. X. Chen, S. Li and H. K. Liu, *J Mater Chem*, 2009, **19**, 8360-8365.

11. Z. Cui, Y. Huang and X. Guo, *Electrochim Acta*, 2012, **60**, 7-12.

12. S. Ding, J. S. Chen, G. Qi, X. Duan, Z. Wang, E. P. Giannelis, L. A. Archer and X. W. Lou, *J Am Chem Soc*, 2010, **133**, 21-23.

13. a) X. W. Lou, D. Deng, J. Y. Lee and L. A. Archer, *Chem Mater*, 2008, **20**, 6562-6566; b) J. Morales, L. Sánchez, *J. Electrochem. Soc.* **1999**, 146, 1640-1642; c) M. Martos, J. Morales, L. Sánchez, *Electrochimica Acta,* **2000**, 46, 83-89.

14. X. W. Lou, C. M. Li and L. A. Archer, *Adv Mater*, 2009, **21**, 2536-2539.

15. a) X. K. Wang, Z. Q. Li, L. W. Yin, *CrystEngComm* **2013**, 15, 7589-97; b) X. K. Wang, Z. Q. Li, Q. Li, C. B. Wang, A. L. Chen, Z. W. Zhang, R. H. Fan, L. W. Yin, *CrystEngComm* **2013**, 15, 3696-3704; c) Y. Zhao, J. Li, N. Wang, C. Wu, G. Dong and L. Guan, *J Phy Chem C* 2012, 116, 18612-17; d) F. B. Hao, Z. W. Zhang, L. W. Yin, *ACS Appl Mater Interfaces* **2013**, 5, 8337-44.

16. a) C. Li, X. Yin, L. Chen, Q. Li and T. Wang, *J Phys Chem C* 2009, 113, 13438-13442; b) Z. Li, N. Liu, X. Wang, C. Wang, Y. Qi, L. W. Yin, *J Mater Chem* **2012,** 22, 16640-48.

17. Y. Wang and T. Chen, *Electrochim Acta*, 2009, **54**, 3510-3515.

18. Y. Wang, I. Djerdj, B. Smarsly and M. Antonietti, *Chem Mater*, 2009, **21**, 3202-3209.

19. Y. J. Mai, J. P. Tu, X. H. Xia, C. D. Gu and X. L. Wang, *J Power Sources*, 2011, **196**, 6388-6393.

20. H. Yu, X. Rui, H. Tan, J. Chen, X. Huang, C. Xu, W. Liu, D. Y. W. Yu, H. H. Hng, H. E. Hoster and Q. Yan, *Nanoscale*, 2013, **5**, 4937-4943.

21. K. M. Nam, Y. C. Choi, S. C. Jung, Y.-I. Kim, M. R. Jo, S. H. Park, Y.-M. Kang, Y.-K. Han and J. T. Park, *Nanoscale*, 2012, **4**, 473-477.

22. Q. Li, L. Yin, Z. Li, X. Wang, Y. Qi and J. Ma, *Acs Appl Mater Interfaces*, 2013, **5**, 10975-10984.

23. M. Martos, J. Morales and L. Sa´nchez, *J Mater Chem*, 2002, **12**, 2979-2984.

24. W. Yuan, J. Yan, Z. Tang, O. Sha, J. Wang, W. Mao and L. Ma, *Electrochim Acta*, 2012, **72**, 138-142.

25. H. Wang, L. Xi, J. Tucek, Y. Zhan, T. F. Hung, S. V. Kershaw, R. Zboril, C. Y. Chung and A. L. Rogach, *Nanoscale*, 2013, **5**, 9101-9109.

26. W. Stöber, A. Fink and E. Bohn, *J Colloid Interf Sci*, 1968, **26**, 62-69.

27. G. Yang, D. Gao, Z. Shi, Z. Zhang, J. Zhang, J. Zhang and D. Xue, *J Phys Chem C*, 2010, **114**, 21989-21993.

28. Y. Mao, W. Li, X. Sun, Y. Ma, J. Xia, Y. Zhao, X. Lu, J. Gan, Z. Liu, J. Chen, P. Liu and Y. Tong, *CrystEngComm*, 2012, **14**, 1419-1424.

29. T. Szörényi, L. D. Laude, I. Bertóti, Z. Kántor and Z. Geretovszky, *J Appl Phys*, 1995, **78**, 6211-6219.

30. O. Y. Khyzhun, T. Strunskus and Y. M. Solonin, *J Alloy Compd*, 2004, **366**, 54-60.

31. M. Chen, X. Wang, Y. H. Yu, Z. L. Pei, X. D. Bai, C. Sun, R. F. Huang and L. S. Wen, *Appl Surf Sci*, 2000, **158**, 134-140.

32. D. Shuttleworth, *J Phys Chem*, 1980, **84**, 1629-1634.

33. W. E. Morgan and J. R. Van Wazer, *J Phys Chem*, 1973, **77**, 964-969.

34. A. W. C. Lin, N. R. Armstrong and T. Kuwana, *Analytical Chemistry*, 1977, **49**, 1228-1235.

35. T. Weber, J. C. Muijsers, J. H. M. C. van Wolput, C. P. J. Verhagen and J. W. Niemantsverdriet, *J Phys Chem*, 1996, **100**, 14144-50.

36. H. Liu, D. Long, X. Liu, W. Qiao, L. Zhan and L. Ling, *Electrochim Acta*, 2009, **54**, 5782-5788.

37. G. L. Xu, S. R. Chen, J. T. Li, F. S. Ke, L. Huang and S. G. Sun, *J Electroanal Chem*, 2011, **656**, 185-191.

38. R. Demir-Cakan, Y.-S. Hu, M. Antonietti, J. Maier and M.-M. Titirici, *Chem Mater*, 2008, **20**, 1227-1229.

39. X. W. Lou, J. S. Chen, P. Chen and L. A. Archer, *Chem Mater*, 2009, **21**, 2868-2874.

40. Z. Wen, Q. Wang, Q. Zhang and J. Li, *Adv Funct Mater*, 2007, **17**, 2772-2778.

41. H. S. Zhou, S. M. Zhu, M. Hibino, I. Honma and M. Ichihara, *Adv Mater*, 2003, **15**, 2107-2111.

42. H. Liu, G. Wang, J. Liu, S. Qiao and H. Ahn, *J Mater Chem*, 2011, **21**, 3046-3052.

Figure captions

Fig. 1 (a) Wide-angle XRD patterns and (b) magnified (110) peak of MTO samples.

Fig. 2. XPS spectra of MTO-1 sample. (a) Survey spectrum, (b) O 1s, (c) Sn $3d_{5/2}$, and (d) Mo 3d.

Fig. 3 (a) N_2 adsorption-desorption isotherms and (b) pore size distribution of MTO samples.

Fig. 4 SEM images of (a) (b) SiO_2 spheres, (c) (d) MTO-0, (e) (f) MTO-1, (g) (h) MTO-2 samples.

Fig. 5 EDS spectrum of MTO-1 sample.

Fig. 6 (a) SEM image of MTO-1 sample. (b) (c) (d) Mo, Sn, O elemental mapping images of MTO-1.

Fig. 7 (a) (b) Low magnification TEM images of MTO-1 sample. (c) A typical electron diffraction (ED) pattern. (d) (e) HRTEM lattice images of the MTO-1 sample suggests that the MTO-1 sample is composed of highly crystalline nanoparticles with a diameter of 3-4 nm. (f) A typical lattice HRTEM image taken along [212] zone axis. The marked d-spacing of 2.12 Å and 2.65 Å corresponds well with that of (1-20) and (-101) planes of tetragonal rutile SnO_2.

Fig. 8 The initial five charge-discharge curves between 0.01 V and 3 V at the current of 100 mAg^{-1} for the MTO anode electrodes: (a) MTO-0; (b) MTO-1 and (c) MTO-2 samples.

Fig. 9 Cyclic voltammetric (CV) curves of the first five cycles between 0.01-3.0 V for the MTO anode electrodes: (a) MTO-0, (b) MTO-1, (c) MTO-2 samples.

Fig. 10 The Nyquist plots of the MTO samples.

Fig. 11 Capacity vs. cycle number curves of the MTO anode electrodes.

Fig. 12 The coulombic efficiency of the MTO-1 anode electrodes for lithium ion batteries.

Fig. 13 Rate capacity for the MTO anode electrodes.

Figure 1

Figure 2

14
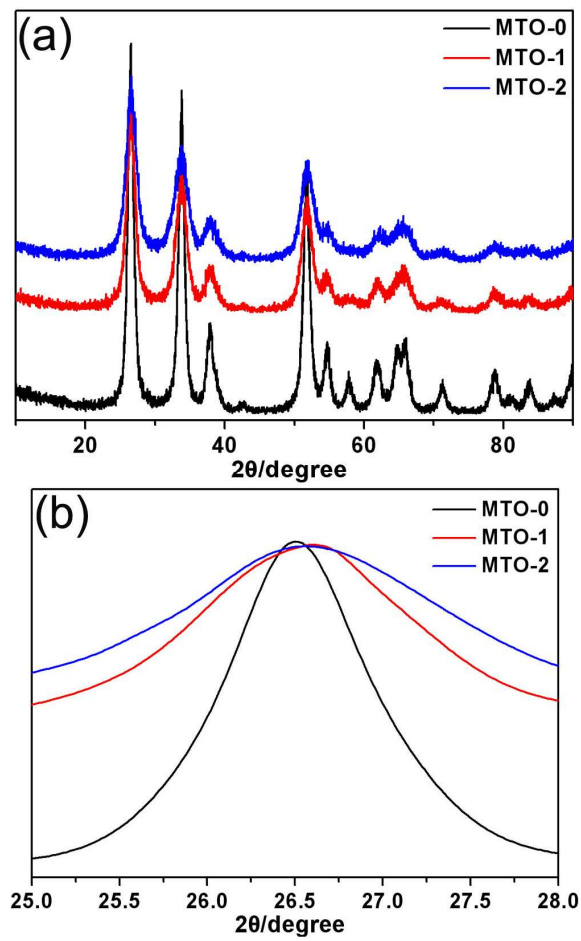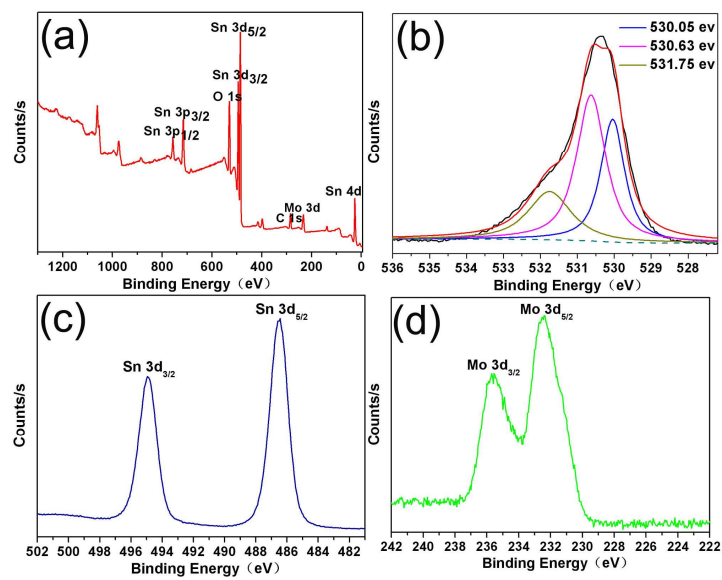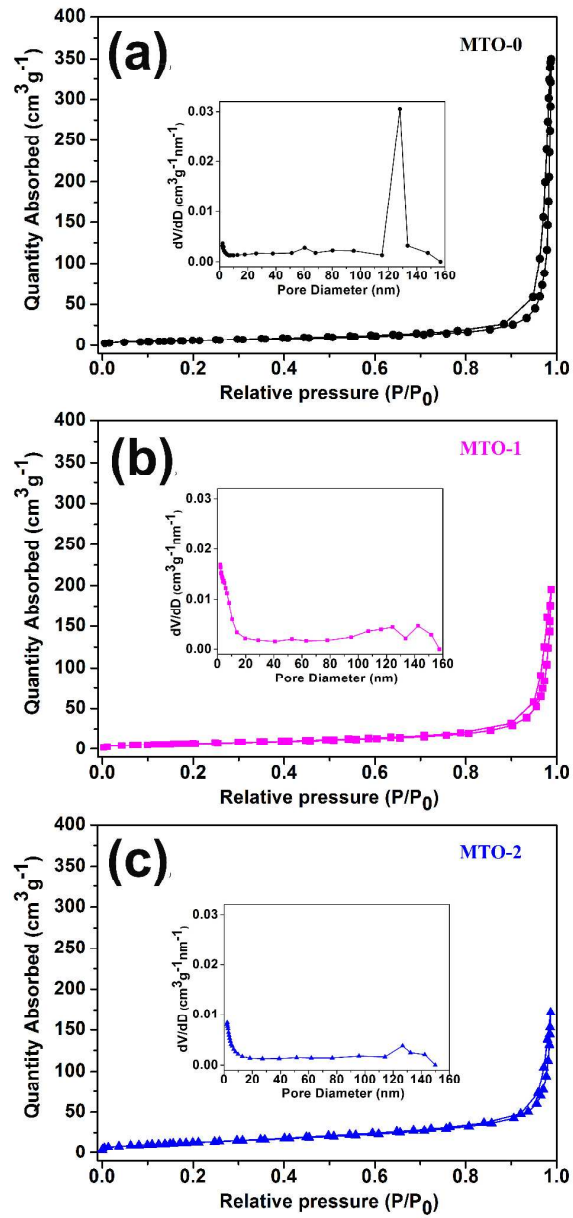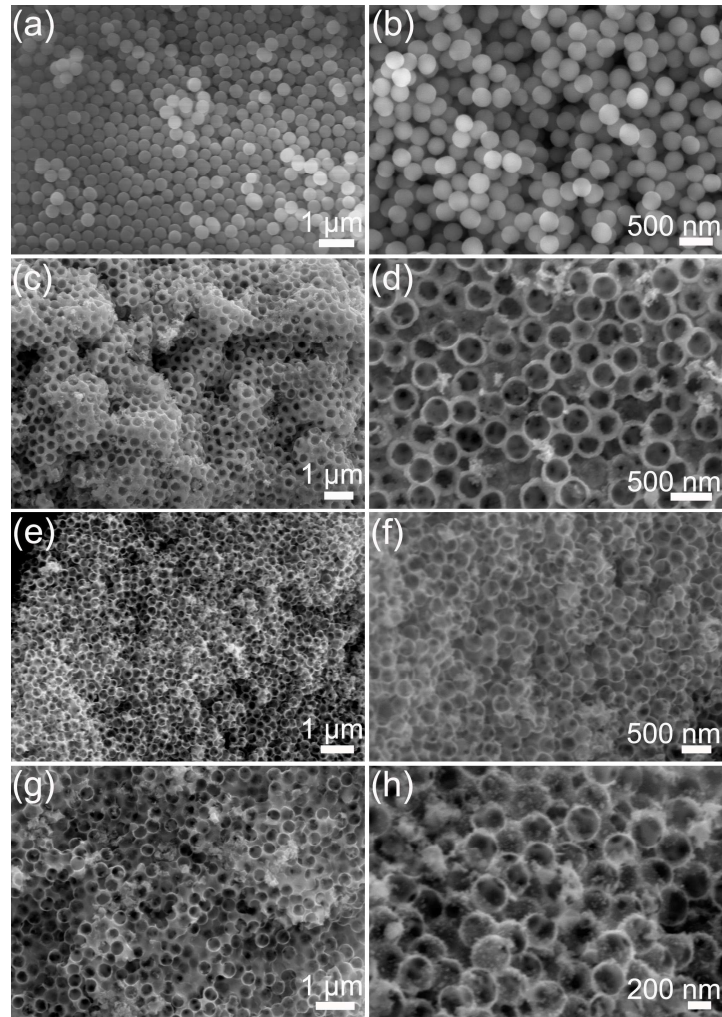
Figure 3

Figure 4

Figure 5
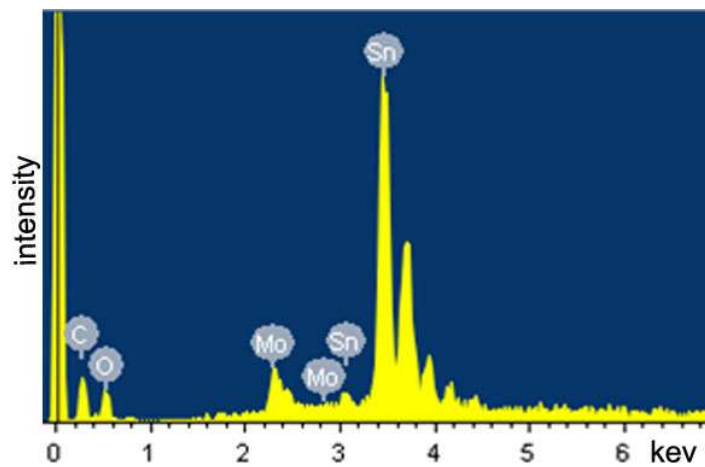
Figure 6
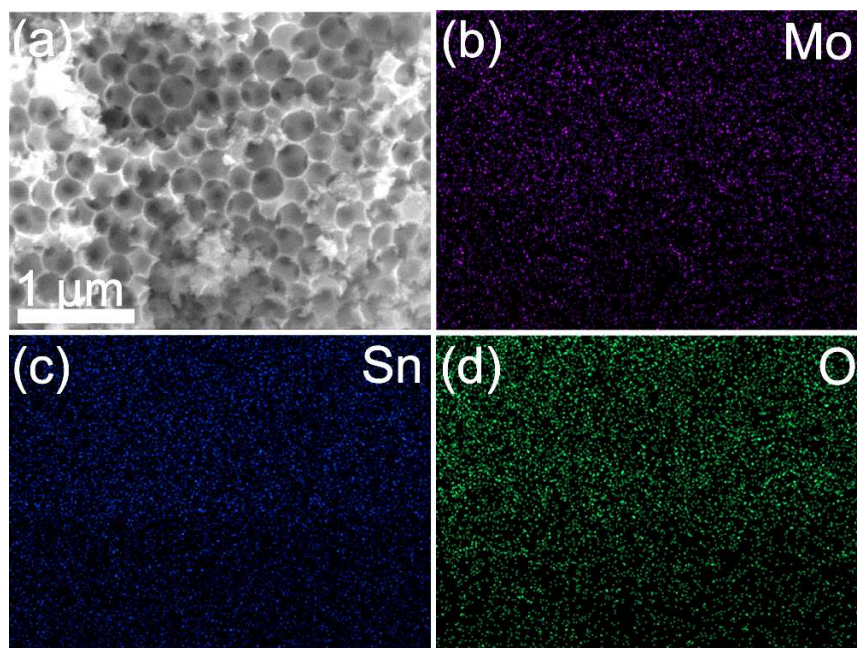
Figure 7
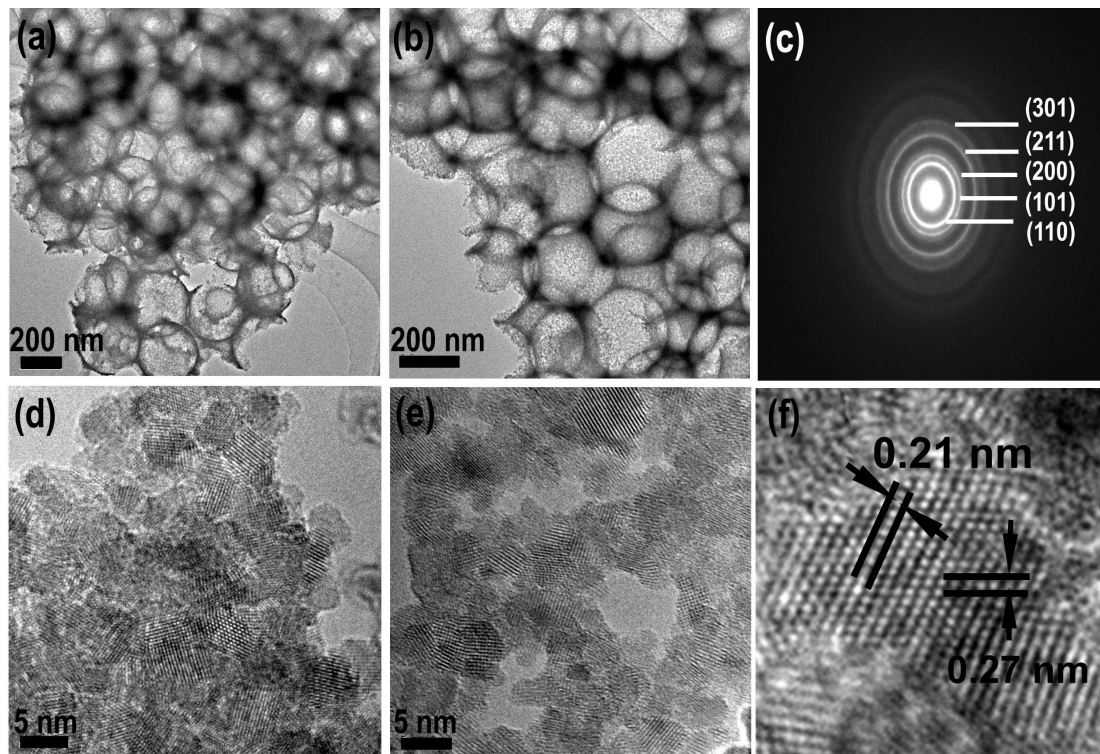
Figure 8
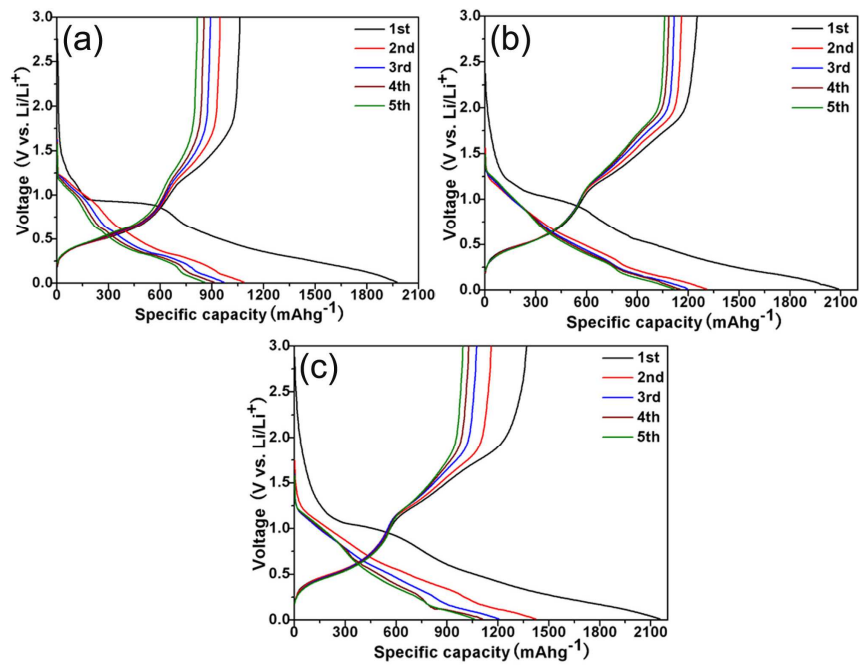
Figure 9
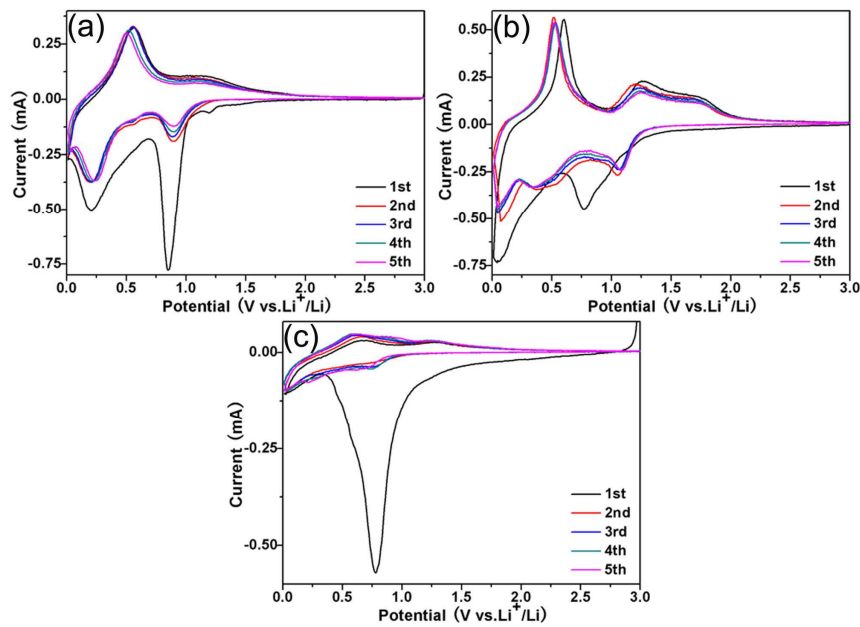
Figure 10
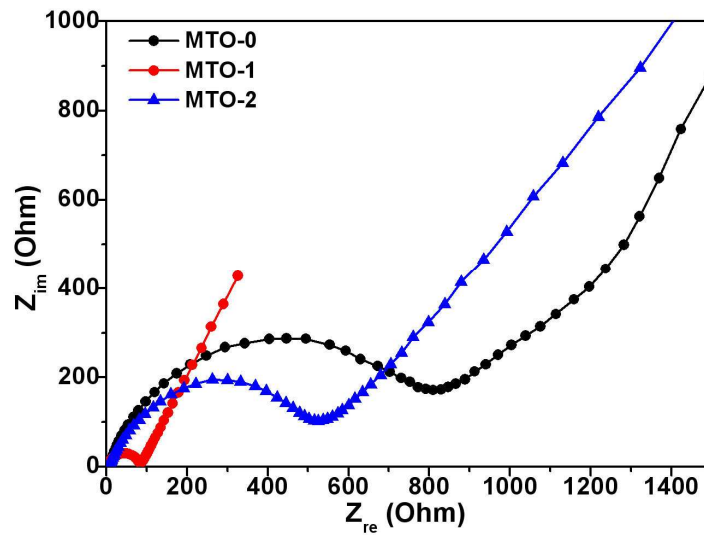
Figure 11
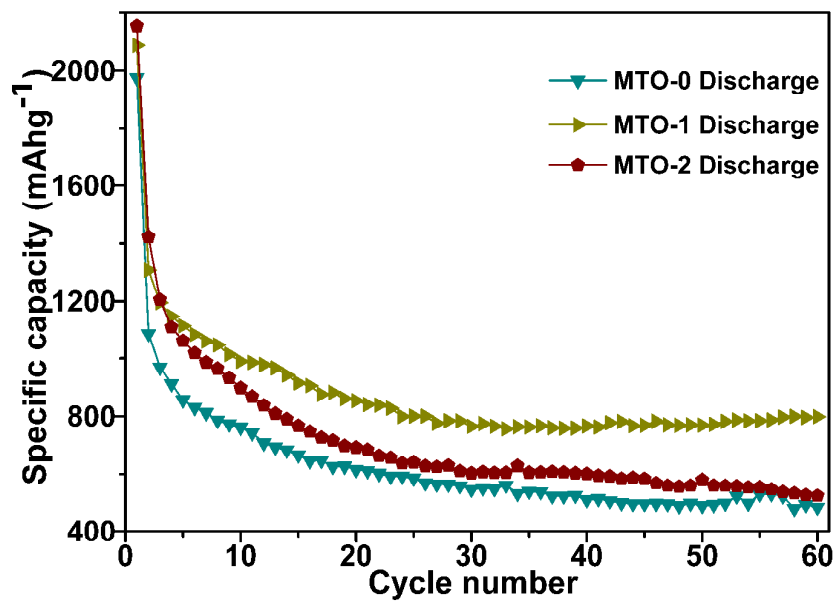
Figure 12
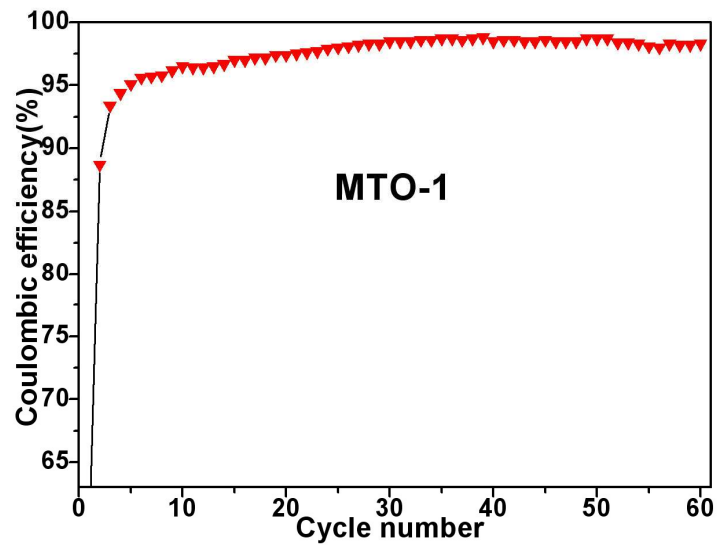
Figure 13
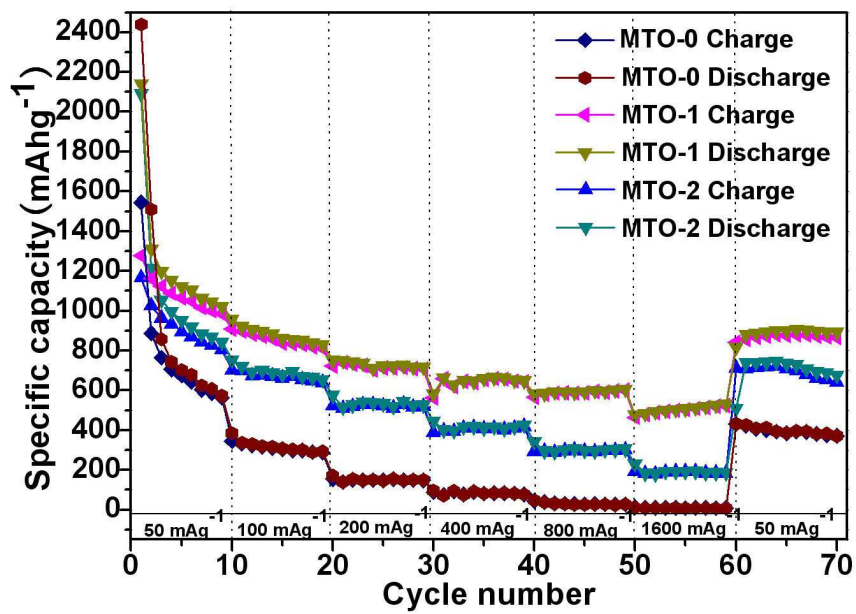
Table 1 The textural properties of MTO samples.

Samples	Surface area $(m^2\,g^{-1})$	Pore size (nm)	Pore volume $(cm^3\,g^{-1})$
MTO-0	26.20	38.39	0.30
MTO-1	103.31	16.91	0.46
MTO-2	48.72	22.13	0.26

Table 2 Unit cell parameters of MTO samples.

Samples	a (Å)	c (Å)	V (Å^3)
MTO-0	4.7467	3.1839	71.74
MTO-1	4.7432	3.1800	71.54
MTO-2	4.7357	3.1841	71.40